

Strain and ligand effect on the electronic structure of Ni-Fe and Ni-Cu alloys: Exploring charge redistribution from x-ray spectroscopies and the charge compensation model

Zeel Patel, Lu Yao, Zhiqiang Wang, Yun Mui Yiu, Tsun-Kong Sham, Sarah Purdy, Jianfeng Zhu, and Sammynaiken Ramaswami

Citation: Chin. Phys. B, 2026, 35 (**5**): 056101. DOI: 10.1088/1674-1056/ae3691
http://cpb.iphy.ac.cn; http://iopscience.iop.org/cpb

What follows is a list of articles you may be interested in

Physical properties of high-pressure synthesized $Al_{65}Cu_{20}Fe_{15}$ quasicrystal

Yibo Liu(刘一博), Changzeng Fan(范长增), Zhefeng Xu(许哲峰), Ruidong Fu(付瑞东), Feng Ke(柯峰), Lin Wang(王霖), Bin Wen(温斌), Lifeng Zhang(张立峰), Marek Mihalkovič, and Bo Xu(徐波)

Chin. Phys. B, 2025, 34 (**9**): 096103. DOI: 10.1088/1674-1056/add4fb

Theoretical characterization of the adsorption configuration of pyrrole on Si(100) surface by x-ray spectroscopy

Hao-Qing Li(李好情), Jing Ming(明静), Zhi-Ang Jiang(姜志昂), Hai-Bo Li(李海波), Yong Ma(马勇), and Xiu-Neng Song(宋秀能)

Chin. Phys. B, 2024, 33 (**2**): 026102. DOI: 10.1088/1674-1056/aceaeb

Temperature-dependent structure and magnetization of $YCrO_3$ compound

Qian Zhao(赵前), Ying-Hao Zhu(朱英浩), Si Wu(吴思), Jun-Chao Xia(夏俊超), Peng-Fei Zhou(周鹏飞), Kai-Tong Sun(孙楷橦), and Hai-Feng Li(李海峰)

Chin. Phys. B, 2022, 31 (**4**): 046101. DOI: 10.1088/1674-1056/ac2b23

Characterization of structural transitions and lattice dynamics of hybrid organic-inorganic perovskite $CH_3NH_3PbI_3$

Feng Jin(金峰), Jian-Ting Ji(籍建亭), Chao Xie(谢超), Yi-Meng Wang(王艺朦), Shu-Na He(贺淑娜), Lei Zhang(张磊), Zhao-Rong Yang(杨昭荣), Feng Yan(严锋), Qing-Ming Zhang(张清明)

Chin. Phys. B, 2019, 28 (**7**): 076102. DOI: 10.1088/1674-1056/28/7/076102

Atomic pair distribution function method development at the Shanghai Synchrotron Radiation Facility

Xiao-Juan Zhou(周晓娟), Ju-Zhou Tao(陶举洲), Han Guo(郭瀚), He Lin(林鹤)

Chin. Phys. B, 2017, 26 (**7**): 076101. DOI: 10.1088/1674-1056/26/7/076101

SPECIAL TOPIC — John Tse: Pioneer in high-pressure materials science

Strain and ligand effect on the electronic structure of Ni–Fe and Ni–Cu alloys: Exploring charge redistribution from x-ray spectroscopies and the charge compensation model

Zeel Patel[1], Lu Yao[1], Zhiqiang Wang[1], Yun Mui Yiu[1], Tsun-Kong Sham[1,†], Sarah Purdy[2], Jianfeng Zhu[2], and Sammynaiken Ramaswami[2]

[1] *Department of Chemistry, Western University, London ON, Canada N6A 5B7*
[2] *Saskatchewan Structural Science Centre, University of Saskatchewan, Saskatoon SK Canada S7N 5C9*

(Received 3 November 2025; revised manuscript received 25 December 2025; accepted manuscript online 12 January 2026)

Nickel-based bimetallic alloys are considered thermally and structurally stable, while also possessing desirable catalytic and magnetic functionalities and being highly abundant and affordable. The electronic structure of such alloys is of particular interest from the perspective of atomic size mismatch and elemental crystal structure compatibility. In this study, we utilize x-ray techniques, including x-ray diffraction (XRD), x-ray absorption spectroscopy (XAS), and x-ray photoelectron spectroscopy (XPS), to understand the strain and ligand effects on charge redistribution upon alloying. We investigate the elemental crystal structures for incompatible alloys of Ni (fcc) and Fe (bcc), and the compatible crystal structure of Ni (fcc) and Cu (fcc) for comparison. Emphasis is placed on interpreting the metal 2p XPS binding energy shift in binary alloys, where one element is diluted into the other, based on the framework of strain and ligand effects and the charge compensation model of Watson et al. Of interest are the different "compressibilities" of the 4s and 3d wavefunctions within the Wigner–Seitz volume, V_{WS}, and the volume-strain effect resulting in intra-atomic 4s–3d rehybridizations within the alloy, as well as the chemical intuition of charge transfer based on the ligand effect (electronegativity). These considerations provide perspective on "internal pressure" due to the strain effect and help in understanding the x-ray data and their correlation with the electronic structures and properties of bimetallic alloy systems.

Keywords: bimetallic alloys, strain and ligand effect, renormalized atom, charge compensation model, x-ray spectroscopy, Mössbauer spectroscopy

PACS: 61.05.C–, 61.05.cj, 73.61.At

DOI: 10.1088/1674-1056/ae3691 **CSTR:** 32038.14.CPB.ae3691

1. Introduction

1.1. General considerations

As novel bimetallic and multielement high-entropy materials with desired functionalities continue to emerge,[1–4] it is desirable to revisit the electronic structure of bimetallic alloys. Ni is of particular interest due to its thermal and structural stability,[5] abundance, and low cost. Ni catalysts used in hydrogen production through methane steam reforming reactions[6,7] inevitably suffer from carbon deposition. Ni–Fe alloys have been determined to exhibit superior catalytic performance in terms of activity (hydrogen production) and stability (resistance to carbon deposition).[8,9] Invar, a Ni–Fe bimetallic material with $\sim 36\%$ Ni, exhibits an exceptionally low coefficient of thermal expansion resulting from the formation of unique magnetic phases.[10,11] The difference in atomic sizes between Ni and Fe leads to strain effects that must be included in the discussion of the electronic structure of these alloys. By contrast, Ni and Cu have similar atomic sizes and provide a counterexample for consideration. The electronic structure of the Ni–Fe and Ni–Cu alloys is examined through the lens of two key phenomena: the strain effect and the ligand effect.

The strain effect considers atomic size mismatch and elemental crystal structure compatibility, especially in the Ni–Fe series where noticeable atomic size and lattice mismatch exist at ambient temperature; Ni is face- centered cubic (fcc), whereas Fe is body-centered cubic (bcc). The Ni–Cu alloys have compatible elemental crystal structures, as both Ni and Cu adopt an fcc crystal structure at room temperature.[12] The strain effect is observed using x-ray diffraction (XRD) patterns and extended x-ray absorption fine structure (EXAFS). The strain effect on the crystal structure is examined in terms of compression/expansion of the lattice constant, hence the atomic volume of the diluted constituent in the alloy relative to the pure element: the volume of the Wigner–Seitz (WS) cell, V_{WS}.[13–19]

The ligand effect is governed by the difference in electronegativity between the alloying elements, which influences charge transfer behavior.[20] The overall effect on electron redistribution in the alloy is observed using x-ray photoelec-

†Corresponding author. E-mail: tsham@uwo.ca

© 2026 Chinese Physical Society and IOP Publishing Ltd. All rights, including for text and data mining, AI training, and similar technologies, are reserved.

tron spectroscopy (XPS) core-level binding energy shifts, as well as x-ray absorption near-edge structure (XANES), which probes the unoccupied density of states (DOS) above the Fermi level. However, the ligand effect alone does not always adequately describe transition metals in the interpretation of XPS core-level shifts, as electronegativity does not distinguish between the nature of the charge, such as 4s vs. 3d, 5s vs. 4d, and 6s vs. 5d in transition metals.[21–25] For example, considering the 4s and 3d electron counts at the Fe site, each can screen the nucleus and the core electron/hole differently. These parameters are affected by volume change (strain) and charge transfer (ligand effect) upon alloying and can be observed in XPS[26] and Mössbauer spectra.[27–29]

1.2. Renormalized atom in a crystal

In a crystal, atomic wavefunctions, and therefore all interactions, such as the Coulomb interaction between a core electron and a valence electron (which determines the core-level binding energy shift), should be normalized within $V_{\rm WS}$.[15–17] For example, the radial part of the 4s wavefunction in a free Ni atom is more diffuse than the 3d wavefunction, and renormalization of the radial wavefunction from zero to the WS radius increases the disparity of the Coulomb interaction between the levels of interest. The renormalized Slater integrals $F(2{\rm p},3{\rm d})$ and $F(2{\rm p},4{\rm s})$ have noticeably different values.[15–17] These values are typically on the order of ~ 10 eV, where the Slater integral $F(i,n)$, with i and n being the core and the valence electrons, respectively, has the form

$$F(i,n) = \iint P_i^2(r_1)\frac{1}{r_>}P_j^2(r_2)r_1^2\,{\rm d}r_1 r_2^2\,{\rm d}r_2,$$

where $r_>$ is the greater of the two radial coordinates r_1 and r_2, and $P_i(r)$ and $P_j(r)$ are the radial components of the one-electron orbitals i and j, such as 2p and 3d/4s, respectively.

This result is important in the interpretation of XPS core-level binding energy shifts because it tracks the effect of gaining or losing a valence electron (s or d) on the core-level binding energy shift. The renormalization introduces a "pressure effect" on the s and d wavefunctions, leading to an increase in the Coulomb interaction and intra-atomic rehybridization of the s and d orbitals, which can change the s and d electron counts when both are "compressed." Intra-atomic s–d rehybridization may become more favorable, with s-to-d redistribution where the occupancy of the more diffuse 4s states (occupied DOS in the conduction band) decreases and the 3d count increases. This is why the valence electronic configurations of Fe and Ni metals are better considered as $4{\rm s}^1 3{\rm d}^7$ and $4{\rm s}^1 3{\rm d}^9$ instead of $4{\rm s}^2 3{\rm d}^6$ and $4{\rm s}^2 3{\rm d}^8$, respectively, in free atoms. In fact, general band theory indicates that 3d metals, Ti through Ni, are well described by $4{\rm s}^1 3{\rm d}^{n+1}$.[16]

The model presented by Watson *et al.*[19] invokes intra-atomic rehybridization (s to d or d to s) and charge compensation (e.g., loss in d is compensated by a gain of s), with a very small overall charge transfer at the site of a metal atom in the alloy.[19,30] This model has resolved many apparently counterintuitive experimental anomalies in XPS binding energy shifts and Mössbauer isomer shifts and quadrupole splitting, for which the interpretation often relied on electronegativity considerations and free- atom wavefunctions, especially in 5d noble metals such as Au and Pt alloys.[21–25] For example, Au is the most electronegative metallic element and Al is highly electropositive; Au is expected to gain charge in $AuAl_2$, yet the Au $4{\rm f}_{7/2}$ level exhibits a large positive chemical shift in $AuAl_2$ ($+1.7$ eV).[20] In Au–Pt alloys, Au and Pt are the most and second-most electronegative elements, respectively, and the $4{\rm f}_{7/2}$ levels of both Au and Pt exhibit negative shifts in the alloys.[22] It is also interesting to note that Ni $2{\rm p}_{3/2}$ in $NiAl_3$ exhibits a positive binding energy shift of $+1.0$ eV, in contrast to electronegativity predictions (Ni is more electronegative than Al).[31]

When an alloy is formed, charge redistribution of s and d character occurs in the valence band due to s–d hybridization. Let us consider the change in electron count as $\Delta n_{\rm c}$ and $\Delta n_{\rm d}$, for the occupied conduction band and d-band electron counts, respectively. The net electron transfer δ on or off the site is given by $\delta = \Delta n_{\rm c} + \Delta n_{\rm d}$. Since the alloy maintains local electroneutrality, δ is usually on the order of ~ 0.1 electron.[24,30] This small charge transfer sets up a Madelung-like term, $F({\rm latt})$. These considerations establish the compensation model, which allows us to examine the electronic structure in bimetallic materials in terms of chemical intuition and the ligand effect (electronegativity)[20] if we consider that charge gain is of s character and is compensated by depletion of d charge, or vice versa. A considerable amount of work shows that, in the case of Au alloys, Au gains 6s charge and loses 5d charge, and δ is consistent with electronegativity considerations. This model explains the apparent anomalies in XPS binding energy shifts and is further confirmed by Mössbauer and XANES studies.[29] We explore here how it applies to 3d bimetallic alloys.

In this work, we discuss the interplay of strain and ligand effects on the electronic structure of Ni-based bimetallic alloys revealed by x-ray spectroscopy and Mössbauer spectroscopy in the context of the charge compensation model.[16,19] XRD, Fe, Ni, and Cu XPS 2p binding energies, XAS at the Fe K-edge, and DFT calculations of the Ni–Fe and Ni–Cu d-band DOS were examined. We also revisit previous ^{57}Fe Mössbauer data of Ni–Fe alloys,[28] and valence-band photoemission of Ni–Cu alloys.[26]

1.3. Crystal structure

The lattice constants for Ni, Fe, and Cu are 3.499 Å, 2.857 Å, and 3.597 Å, respectively.[12] The size mismatch

caused by the strain effect is described using V_{WS}. It should be noted that for these 3d elements, the atomic volume in the gas phase exhibits a mini lanthanide contraction; this is not necessarily the case in the solid. It is expected that the structure of Fe diluted in fcc Ni, with Fe replacing some of the Ni, is also fcc; likewise, Ni diluted in bcc Fe is bcc. It is interesting to note, however, that Fe adopts the fcc structure at a composition much higher than 50%. In fact, it becomes fcc at $\sim$ 64% Fe ($\sim$ 36% Ni), which is the Invar composition. It is expected that Fe in Ni-rich fcc alloys will experience compressive strain due to a larger V_{WS} than that of Ni. Similarly, Ni in a bcc Fe lattice will undergo tensile strain. We also investigate the structure of Cu diluted in fcc Ni, and Ni diluted in fcc Cu. We expect tensile strain for Ni in Cu-rich alloys and compressive strain for Cu in Ni-rich alloys, as Cu has a slightly larger V_{WS}. These strain patterns are observed using XRD and EXAFS.

1.4. Characterization through x-ray spectroscopic techniques

Changes in the electronic structure were explored through XPS and x-ray absorption spectroscopy (XAS).

The XPS method measures the kinetic energy, E_K, of electrons emitted from a core level using an x-ray excitation source having energy $h\nu$. The electron must overcome the work function, Φ_{metal}, and the binding energy (BE) is given by

$$\mathrm{BE} = h\nu - E_K - \Phi_{metal}. \tag{1}$$

The work functions for polycrystalline Fe, Ni, and Cu are 4.5 eV, 5.3 eV, and 4.7 eV, respectively.[32] The E_F of the metal and the E_F of the spectrometer are equalized during measurement when the sample is grounded. The work function of the alloy can be estimated using Vegard's law.[14,33]

The binding energy shift represents a change in the electronic structure that depends on the chemical environment of an element in the alloy. In the alloys discussed here (3d metals), the binding energy shifts of the 2p core levels provide insight into charge redistribution when comparing the spectra of the unalloyed and alloyed materials, since they have narrow core-lifetime broadening widths (long core-hole lifetimes), hence higher chemical sensitivity. To study charge redistribution, the binding energy shift and the line shapes between the metal and alloy core levels are compared. The binding energy shift in $2p_{3/2}$ between Ni in an alloy and Ni in the Ni metal, for example, analogous to the Au alloy cases, can be expressed as[19]

$$\begin{aligned}\Delta \mathrm{BE}_{\text{alloy-metal}} = &-\left(\Phi_{\text{alloy}} - \Phi_{\text{m}}\right) - \Delta n_{\text{c}} F\left(2p_{3/2}, n_{\text{c}}\right) \\ &-\Delta n_{\text{d}} F\left(2p_{3/2}, 3\text{d}\right) + \delta F\left(\text{latt}\right) + \left[\frac{\mathrm{dBE}}{\mathrm{d}V}\Delta V\right].\end{aligned} \tag{2}$$

In the first term, Φ_{alloy} can be obtained from Vegard's law and is $\sim \pm 0.5$ eV for these alloys.[14,33]

The most important terms in determining the binding energy shift are the Coulomb interactions between a conduction electron and a d electron with the core electron of interest, represented by the Slater integrals $F(2p_{3/2}, n_c)$ and $F(2p_{3/2}, 3d)$ in Eq. (2), respectively. The third term usually has a larger effect than the second. Thus, the values of these terms, together with the changes in electron counts upon alloying, Δn_c and Δn_d, not δ alone, determine the BE shift.

In the fourth term, δ is the sum of the change in conduction electron count Δn_c (4s character) and the d-electron count Δn_d. The charge transfer depends on the difference in electronegativity between the constituent elements and is usually very small in alloys. Electronegativity considerations alone can often be problematic in interpreting binding energy shifts of core levels in d-band metals and alloys because they do not distinguish between contributions from s and d electrons in their interaction with core electrons. The next variable in the fourth term, $F(\text{latt})$, is the Madelung term due to the small charge imbalance at the site following charge transfer on and off the WS cell.

The last term in Eq. (2) is related to the strain effect. In general, a compressed site contributes to better screening, lowering the binding energy in XPS and increasing charge density at the nucleus, as determined by ^{57}Fe Mössbauer isomer shifts.

XAS uses photons to excite core electrons to unoccupied electronic states above the Fermi level via bound-to-bound dipole transitions. Additionally, bound-to-continuum transitions beyond the absorption edge are observed, where oscillations in the absorption coefficient arise from the local environment. XAS is often divided into two regions: XANES, which spans energies 20 eV below and 30 eV above the edge, and EXAFS, which extends from 30 eV to as much as 1000 eV above the edge.[34] XANES is used to probe the unoccupied bands above the Fermi level and the local environment of an atom in the metal due to multiple scattering favored by low-energy photoelectrons.[35] XANES probes the unoccupied DOS above E_F.[35] EXAFS (high-energy electrons) favors single scattering and provides information on the interatomic distances between the absorbing atom and its neighboring atoms.

2. Methodology

2.1. Sample preparation

For the Ni–Fe series, two alloy foils with compositions of $Ni_{64}Fe_{36}$ (fcc) and $Ni_{4.5}Fe_{95.5}$ (bcc), as well as pure Fe and Ni metals, were studied. Alloy samples were prepared as ingots by repeatedly melting stoichiometric amounts of the components in an arc furnace, as described previously.[36] The ingots

were then rolled into foils. For Ni–Cu, foils with alloy compositions of $Ni_{90}Cu_{10}$ and $Ni_{10}Cu_{90}$, prepared in a similar way to the Ni–Fe series, as well as pure metal foils, were analyzed.[37] The stoichiometric compositions on their respective phase diagrams ensure that the alloys have the desired phases, as confirmed by XRD (Fig. 1).[38]

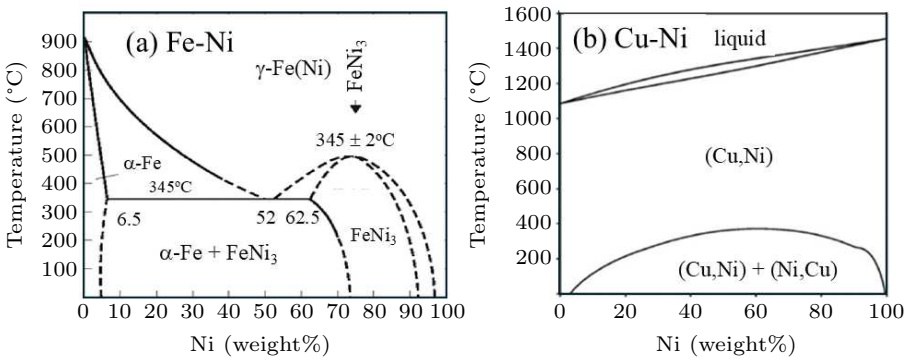


Fig. 1. Binary phase diagram of (a) Ni–Fe and (b) Ni–Cu.

2.2. Powder x-ray diffraction

XRD analyses were performed using the Rigaku Ultima IV x-ray diffractometer, located at the Saskatchewan Structural Sciences Centre (SSSC) at the University of Saskatchewan. A Cu source (1.54 Å), CBO optics, and a scintillation counter detector were equipped on the diffractometer. The measurements were performed using the multipurpose attachment in parafocusing mode, with the foil samples placed on top of the sample plate. The diffraction angles (2θ) were scanned from 30° to 100°, with a scan rate of 1° per minute and a step size of 0.01°.

2.3. X-ray photoelectron spectroscopy

XPS analyses were performed on the Kratos AXIS Supra spectrometer, located at Surface Science Western, using a monochromatic Al $K\alpha$ x-ray source (1486.6 eV). The spectrometer work function was calibrated using Au $4f_{7/2}$ of Au metal at 83.95 eV, and the spectrometer was calibrated to a binding energy of 932.63 eV (Cu $2p_{3/2}$). Additional XPS measurements were performed at SSSC, with results confirming the SSW findings; more details will be reported elsewhere. The samples were sputtered using Ar^+ to remove any oxides present. High-resolution spectra of Ni, Cu, and Fe were collected using a pass energy of 10 eV and a step size of 0.1 eV. Spectral fitting was performed using CasaXPS software.[39]

2.4. X-ray absorption spectroscopy

XAS data were collected on Sector 20-ID at the Advanced Photon Source (CLS@APS) via remote operation. The XAFS spectra of the samples were recorded with two scans in transmission mode at the K-edge of both Fe and Ni. ΔE in the XANES region was 0.3 eV. In the EXAFS region, the Δk, maximum k, and k weight were 0.05 $Å^{-1}$, 15 $Å^{-1}$, and 0.5, respectively. The integration time in both XANES and EXAFS was 1 second. The two scans at each absorption edge were merged and analyzed with ATHENA.[40] EXAFS spectra were Fourier transformed to R space with a k^2 weighting.

2.5. Band structure and densities of states (DOS) calculations

We have conducted band structure calculations of the DOS of Fe, Ni, and Cu, and the 50–50 alloys of Ni–Fe and Ni–Cu using density functional theory (DFT)[41] based on the WIEN2k code.[42] The WIEN program calculates the ground state of the alloys using the linearized augmented plane wave (LAPW) method. The calculations started with model crystals and alloys, where we used CIF files of bcc Fe, fcc Ni, and fcc Cu from the Materials Project.[43,44] The 50–50 alloys were constructed using $2 \times 2 \times 2$ supercells, with half of the atoms replaced by the other metal. We employed the generalized gradient approximation (GGA).[45] Relativistic effects for valence states were included using a scalar relativistic treatment, while core states were treated fully relativistically. The systems were then calculated by self-consistent iterations until the minimum energy of the ground state was reached, with an energy convergence criterion of 0.0001 Ry. The number of k-points was 1000, and magnetic structure was not considered. We used the PBE–GGA as the exchange–correlation potential.[46] The partial densities of states (DOS) of Fe, Ni, and Cu were calculated based on the distribution of the eigenstates of these ground states.

3. Results and discussions

3.1. Strain effect from XRD: The long-range order

Upon alloy formation, it is expected that the lattice parameters will change following Vegard's law.[14,33] Examination of V_{WS} of the alloys provides an average volume per atom in the solid. This is compared to the volume of the unalloyed components to determine which atoms are under compressive or tensile strain. The differences in V_{WS} provide insight into

the expected influence on electron binding energy in the absence of charge transfer, allowing for assessment of the significance of the strain effect. The XRD patterns and the shifts of the Bragg peaks show that when Ni is diluted in Fe, the alloy adopts a bcc structure, and when Fe is diluted in Ni, it adopts an fcc structure, as seen in Fig. 2(a), whereas all Ni–Cu alloys are fcc (Fig. 2(b)). The unit cell dimensions are calculated from the average of the first three low-index peaks. The V_{WS} values are calculated based on the unit cell volume, and all relevant results are summarized in Table 1.

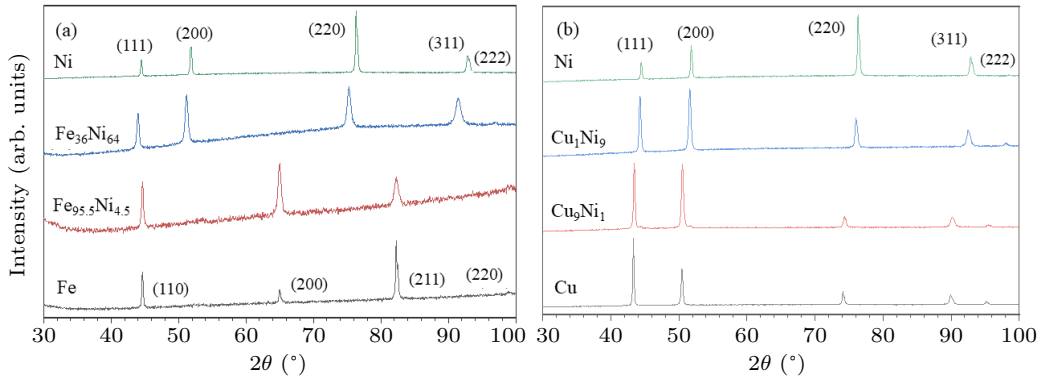


Fig. 2. XRD patterns of the Ni–Fe series. (a) Fe foil, $Fe_{95.5}Ni_{4.5}$ alloy, $Fe_{36}Ni_{64}$ alloy, and Ni foil, and the Ni–Cu series. (b) Ni, $Ni_{10}Cu_{90}$, $Ni_{90}Cu_{10}$, and Cu foil. The shifts are apparent in the high-index peaks. The variation in the intensity of the Bragg peaks is due to texture effects, as all samples are thin foils and those of the alloys were rolled from ingots.

Table 1. Diffraction peaks and calculated unit cell dimensions (averaged lattice parameter) and V_{WS} corresponding to the Ni–Fe and Ni–Cu series (Fig. 2).

Samples	Diffraction peaks at 2θ (°)			Calculated unit cell (Å)	Standard deviation (Å)	V_{WS} (Å^3)
	(111)	(200)	(220)			
Pure Ni	44.47	51.82	76.33	3.526	0.0004	10.95
$Ni_{64}Fe_{36}$	43.96	51.9	75.27	3.567	0.0017	11.31
	(110)	(200)	(211)			
Pure Fe	44.67	64.99	82.30	2.867	0.0011	11.78
$Fe_{95.5}Ni_{4.5}$	44.66	64.98	82.28	2.867	0.0013	11.78
	(111)	(200)	(220)			
Pure Ni	44.47	51.82	76.33	3.526	0.0004	10.95
$Ni_{90}Cu_{10}$	44.30	51.61	76.04	3.538	0.0014	11.07
$Ni_{10}Cu_{90}$	43.42	50.54	74.32	3.608	0.0012	11.80
Pure Cu	43.31	50.44	74.12	3.625	0.0002	11.92

Let us first consider the Ni–Fe series. From Fig. 2 and Table 1, we see that Ni ($Z = 28$), the closest packed metal, has a smaller V_{WS} than that of Fe ($Z = 26$). The $Ni_{64}Fe_{36}$ alloy, where Fe is diluted in Ni, is observed to have a fcc lattice with a smaller Fe atomic volume than Fe in Fe metal. Fe is compressed in the alloy, while Ni is subjected to tensile strain. For the $Ni_{4.5}Fe_{95.5}$ alloy, the structure is bcc and Ni is a small minority component. The lattice constant and V_{WS} of Fe in the alloy remain close to those of pure Fe. This observation suggests that Fe diluted in fcc Ni tends to retain its V_{WS} in pure Fe.

When Ni is diluted in bcc Fe, as in $Fe_{95.5}Ni_{4.5}$, the alloy adopts the bcc structure, and Ni's coordination number is reduced from 12 to 8. The alloy incorporates smaller Ni atoms into a larger Fe lattice site. In this case, the atomic volume of Fe atoms exhibits little change. For the Ni atom in the alloy, there is more room at the atomic site, favoring d-to-s redistribution. The opposite is true when Fe is compressed in fcc Ni, as in $Ni_{64}Fe_{36}$. From the Ni perspective, both alloys undergo tensile strain, as we are incorporating slightly larger Fe atoms into a lattice made of smaller Ni atoms. Fe diluted in fcc Ni has 12 nearest neighbors, so it is compressed compared to the unalloyed bcc Fe with 8. Thus s–d rehybridization in favor of s-to-d redistribution can occur, providing less screening of the nucleus.

In the Ni–Cu series, both Ni and Cu metals have an fcc structure and are completely miscible in Ni–Cu alloys across all compositions. In addition, Ni and Cu have nearly identical electronegativities, so the ligand effect is negligible. When Ni is diluted in Cu, as in $Ni_{10}Cu_{90}$, there is a decrease in the lattice parameter and V_{WS}, as expected. Ni is at the slightly larger atomic site previously occupied by Cu, and s–d rehybridization occurs in favor of d-to-s redistribution. When Cu is diluted in Ni, as in $Ni_{90}Cu_{10}$, there is an increase in the lattice parameter and V_{WS} compared with pure Ni, but a decrease compared with pure Cu, indicating that Cu is compressed.

3.2. Ni and Fe EXAFS of Ni–Fe alloys: The short-range order

The XANES and EXAFS data have been remeasured for the Ni–Fe series.[36] Unlike XRD, EXAFS determines the short-range order, i.e., the interatomic distance of neighboring atoms around the absorbing atoms. Figure 3 shows the XANES and the Fourier transform (FT) of the EXAFS at both the Fe and Ni K-edges of both alloys and the pure metals.

Ni and Fe are close in the periodic table; they have similar k-dependence in phase shift and backscattering amplitude, and hence exhibit similar scattering patterns in both XANES and EXAFS. The XANES results confirm that both

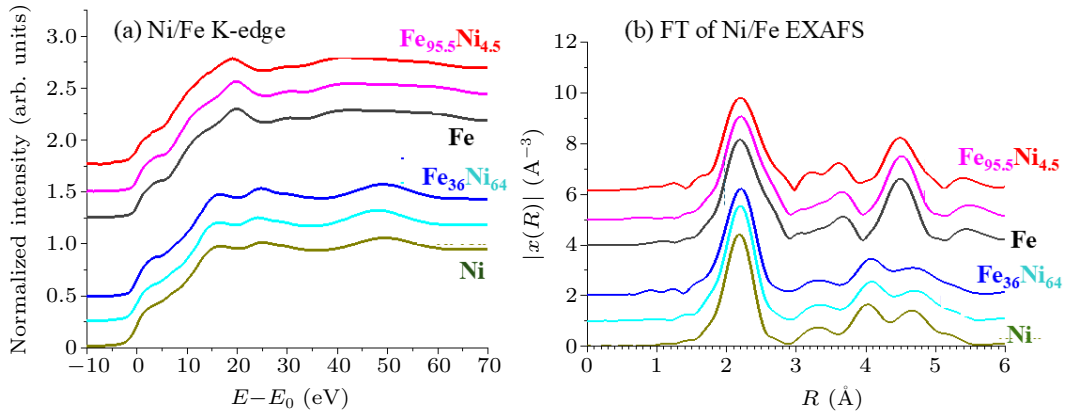


Fig. 3. (a) Fe and Ni K-edge XANES spectra aligned at the K-edge threshold (E_0) for the alloys and the pure metals. The elemental edge XANES spectra are color coded. The upper set of spectra corresponds to Ni diluted in Fe, $Fe_{95.5}Ni_{4.5}$, and the lower set corresponds to Fe diluted in Ni, $Fe_{36}Ni_{64}$. (b) Fourier transform (FT) of the corresponding EXAFS from the same set of spectra.

Ni and Fe in $Fe_{95.5}Ni_{4.5}$ adopt a bcc lattice, showing features similar to those of α-Fe. For $Fe_{36}Ni_{64}$, both Ni and Fe K-edge XANES spectra resemble that of pure Ni, indicating that Fe adopts the fcc structure, as seen at the bottom of Fig. 3(a). The radial distribution from the FT of the EXAFS shown in Fig. 3(b) indicates that the Fe–Ni/Fe interatomic distance increases slightly in the Ni-rich alloy but remains nearly unchanged in $Fe_{95.5}Ni_{4.5}$, where Ni in bcc Fe adopts a V_{WS} similar to that of its Fe host. The average Ni–Fe/Ni and Fe–Ni/Fe distances in $Fe_{36}Ni_{64}$ are the same within experimental uncertainty, but they are longer (+0.023 Å) than the Ni–Ni distance in pure Ni. The average Ni–Fe first-shell distance in $Fe_{95.5}Ni_{4.5}$ is slightly shorter (−0.020 Å) compared with the average Fe–Fe/Ni distance in the alloy and the Fe–Fe distance in pure Fe. Considering the slightly different phase and backscattering amplitude of Ni and Fe and the experimental uncertainty, this interpretation is qualitative but consistent with the XRD observation.

3.3. Strain and ligand effect on the interpretation of XPS $2p_{3/2}$ binding energy shifts and the charge compensation model

Electronegativity is a measure of how well an atom can attract electrons to itself in a chemical environment and is the foundation of chemical intuition in describing charge redistribution upon compound formation.[20] Thus, the electronegativity difference can be used as a chemically intuitive tool to understand electron distribution upon alloy formation, tracking the direction of net charge transfer between Fe (Pauling electronegativity: 1.83) and Ni (Pauling electronegativity: 1.91) in Ni–Fe alloys. In the Ni–Fe system, Ni is more electronegative, drawing electron charge from Fe, and the net charge transfer is expected to occur from Fe to Ni, resulting in a positive shift in Fe $2p_{3/2}$ relative to metallic Fe. In the Ni–Cu system, the electronegativity difference between Ni (1.91) and Cu (1.90) is negligible; therefore, little charge transfer is expected based on the ligand effect in Ni–Cu alloys, and the observed peak shift should be negligible.

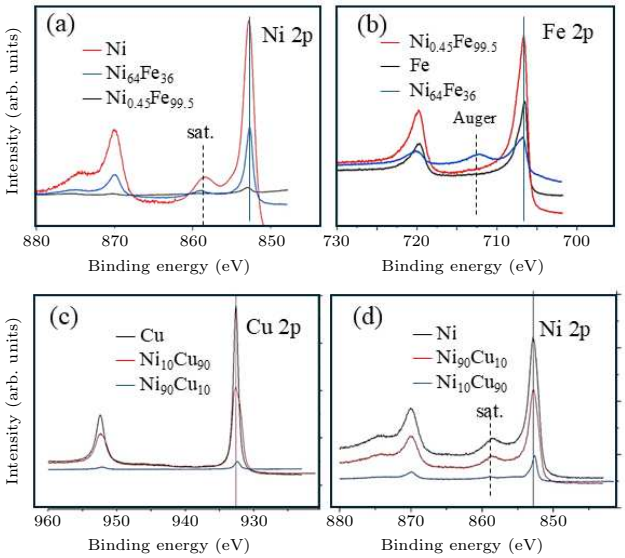


Fig. 4. 2p core-level XPS spectra for the Ni–Fe and Ni–Cu alloy series. (a) Ni 2p for the Ni–Fe series; (b) Fe 2p for the Ni–Fe series; (c) Cu 2p for the Ni–Cu series; and (d) Ni 2p for the Ni–Cu series. The well-known satellite is clearly observed in the Ni spectra at 6.0 eV higher binding energy than that of the main $2p_{3/2}$ peak (marked with a solid line), and is indicated by a dashed line in panels (a) and (c). The Ni LMM Auger structure is observed at 712.2 eV (dashed line), in the higher-energy region of the Fe $2p_{3/2}$ spectrum of the $Ni_{64}Fe_{36}$ alloy in panel (b).

The Fe, Ni, and Cu $2p_{3/2,1/2}$ core-level peaks for each Ni–Fe and Ni–Cu alloy are shown in Fig. 4. The asymmetric Doniach–Sunjić lineshape in the Fe and Ni 2p peaks indicates the presence of unoccupied 3d states at E_F, whereas the Cu 2p spectrum is symmetric, indicating that Cu has a fully occupied d band that lies below the Fermi level, with very few unoccupied 3d states above it. In contrast, in the Fe and Ni 2p spectra, the asymmetry cannot be fully quantified due to a small Δn_d and exchange interactions.[47,48] Their respective $2p_{3/2}$ binding energy shifts are listed in Table 2. It is observed that the Fe $2p_{3/2}$ peaks shift to higher binding energies with dilution in Ni. The Ni $2p_{3/2}$ peaks shift to lower binding energies upon incorporation of Fe, in good agreement with electronegativity predictions.

We expect that Ni withdraws charge from Fe, and the effect of charge transfer is expected to be greater when Fe is more dilute. It is straightforward to show that, on average, the atomic ratio of Fe to Ni in $Fe_{95.5}Ni_{4.5}$ is 21.2:1; with the bcc coordination number of 8 factored in, the average nearest-neighbor environment of Fe consists of 7.6 Fe atoms and 0.36 Ni atoms. This means not all Fe atoms have Ni as a nearest neighbor, and some Ni atoms are entirely surrounded by Fe atoms. Similarly, in $Fe_{36}Ni_{64}$, Fe has on average 7.6 Ni nearest neighbors, among which 4.3 are Fe-related contributions in the local environment. The observed Fe $2p_{3/2}$ shift is positive and increases with dilution (Table 2), consistent with electronegativity considerations. Thus, the ligand effect alone can be used to interpret the trend. In the spirit of Eq. (2), $\delta = \Delta n_c + \Delta n_d$ is negative (loss of electron charge) at the Fe site in Ni–Fe alloys. From the Ni perspective, Ni gains charge and δ is positive, leading to a lowering of the Ni $2p_{3/2}$ binding energy (negative shift relative to Ni metal) as the Ni concentration decreases (Table 2). Thus, the ligand effect alone can explain the trends observed in these Ni–Fe alloys. From XPS core levels alone, however, we cannot determine whether the charge compensation model plays a significant role.

Table 2. Core level ($2p_{3/2}$) binding energy shifts in the Ni–Fe and Ni–Cu alloy series.

Ni–Fe		
Fe $2p_{3/2}$	Binding energy (BE) (eV)	ΔBE (alloy-metal) (eV)
Pure Fe (bcc)	706.3	NA
$Fe_{95.5}Ni_{4.5}$ (bcc)	706.4	0.1
$Fe_{36}Ni_{64}$ (fcc)	706.6	0.3
Ni $2p_{3/2}$	Binding energy (BE) (eV)	
Pure Ni (fcc)	852.9	NA
$Ni_{64}Fe_{36}$ (fcc)	852.7	−0.2
$Ni_{4.5}Fe_{95.5}$ (bcc)	852.6	−0.3
Ni–Cu		
Cu $2p_{3/2}$	Binding energy (BE) (eV)	ΔBE (alloy-metal) (eV)
Pure Cu	932.6	NA
$Ni_{10}Cu_{90}$	932.5	−0.1
$Ni_{90}Cu_{10}$	932.4	−0.2
Ni $2p_{3/2}$	Binding energy (BE) (eV)	
Pure Ni	852.7	NA
$Ni_{90}Cu_{10}$	852.7	0
$Ni_{10}Cu_{90}$	852.7	0

We now examine the strain effect, the $\left[\frac{dBE}{dV}\Delta V\right]$ term in Eq. (2), and consider how it may modify the Fe and Ni 2p shifts. This term arises implicitly from changes in the n_c and n_d counts due to compression and expansion of V_{WS} in the alloy, as compression of the site favors s-to-d rehybridization, while expansion favors d-to-s rehybridization. From the Fe perspective, in the absence of net charge transfer, Fe is compressed when diluted in the Ni lattice; compression favors s-to-d rehybridization and increases the n_d count and decreases the n_c count, albeit slightly, as the atomic volume of Fe is reduced by 4% in $Fe_{36}Ni_{64}$ and 0.4% in $Fe_{99.5}Ni_{4.5}$ (Table 2). This rehybridization alone would decrease the binding energy, as Fe is losing s charge and gaining 3d charge. This is because the Coulomb term F(2p, 3d) is greater than F(2p, 4s). The observed Fe 2p shift is positive, meaning that the ligand effect is more important than the strain effect. From the Ni perspective, its atomic site volume increases by 3.3% in $Fe_{36}Ni_{64}$ and 7.6% in $Fe_{99.5}Ni_{4.5}$ compared with fcc Ni, favoring d-to-s rehybridization. In the absence of charge transfer, this would increase the 4s count and deplete the 3d count; this effect alone is expected to yield a positive Ni 2p binding energy shift. In this case, the observed shift is negative, again indicating that the ligand effect is more important than the strain effect.

We next examine the Ni–Cu results. From Table 2, we see that Cu $2p_{3/2}$ shifts to lower binding energies in the alloy upon increasing composition of the other constituent, while the Ni $2p_{3/2}$ shows no shift within experimental error. The negative shift in Cu is anomalous from a simple consideration, as the electronegativities of Cu and Ni are nearly identical. The data suggest that Cu gains charge. This anomaly can be understood in terms of intra-atomic s-to-d rehybridization.

We now explore lattice strain further. When Ni–Cu alloys are formed, Ni occupies a site about 8% larger in $Ni_{10}Cu_{90}$ and only 1% larger in $Ni_{90}Cu_{10}$, while Cu is compressed, with its volume being 1% and 7% smaller in $Ni_{10}Cu_{90}$ and $Ni_{90}Cu_{10}$, respectively. Thus, if there is no interatomic charge transfer, the tensile strain effect will increase the binding energy of Ni $2p_{3/2}$, while compressive strain will decrease the binding energy of Cu $2p_{3/2}$ in the alloys. The Cu results are consistent with this analysis, while the Ni result shows no shift in the alloy within experimental uncertainty. Since s wavefunctions are more diffuse beyond the WS cell boundary, it is reasonable to expect that compressive strain has a larger effect on s-to-d rehybridization than tensile strain. Another difference is the presence of a fully filled d band in Cu versus a partially filled d band in Ni. The Cu d band edge is below the Fermi level.

3.4. ^{57}Fe Mössbauer isomer shift of Ni–Fe alloys revisited

It is interesting to revisit earlier Mössbauer work and examine whether the strain and ligand effects play a role in understanding these results.[10,28,49] For example, Lehlooh *et al.* reported a Mössbauer study of Fe in NiFe alloys with compositions in the Invar region: $Fe_{70}Ni_{30}$, $Fe_{65}Ni_{35}$, and $Fe_{60}Ni_{40}$.[28] They found that $Fe_{70}Ni_{30}$ is a mixed phase (fcc and bcc), while $Fe_{65}Ni_{35}$ and $Fe_{60}Ni_{40}$ are single phase (fcc), in good agreement with our observation. They observed that the ^{57}Fe isomer shift (IS) changes relative to bcc Fe from the single-phase samples are very small, -0.03 ± 0.01 mms^{-1} ($Fe_{65}Ni_{35}$) and -0.01 ± 0.01 mms^{-1} ($Fe_{60}Ni_{40}$). Since a negative IS corresponds to higher electron density at the nucleus, this implies

that the s charge density increases at the Fe site in these Ni–Fe alloys. This is counterintuitive from electronegativity considerations, as Ni is slightly more electronegative than Fe; thus the increase in s density at the nucleus must be compensated by a decrease in 3d screening via 3d charge depletion, consistent with the XPS results discussed above. It should be noted, however, that these results should ideally be verified using measurements of the same samples with both Mössbauer and x-ray spectroscopy.

3.5. The behavior of the d band of NiFe and NiCu

The DOS of the d band for 50–50 alloys of NiFe and NiCu from DFT calculations are shown in Fig. 5. The DOS of Ni and Fe d character overlap for NiFe with bcc structure, shown in Fig. 5(a). The Ni and Fe 3d bands repel slightly: the Ni d band moves slightly away from the Fermi level, whereas the Fe d band moves towards the Fermi level. This d–d repulsion has a stronger effect in the closely packed fcc Ni–Fe system, where the elemental DOS features are more distinct, as shown in Fig. 5(b). In the NiCu alloy, the Cu d band is fully occupied and lies below the Fermi level, and the d–d repulsion is most apparent in Fig. 5(c). The d–d repulsion for the NiCu alloy (Fig. 5(d)) has been observed in photoemission experiments by Hüfner *et al.*[26]

These results show that, unlike Au–Cu alloys where the Au (5d) and Cu 3d bands are well separated,[21–24] the d bands are more likely to overlap in 3d metal alloys despite mutual repulsion, especially for elements that are close in the periodic table such as Ni, Fe, and Cu. From Fig. 5(d), we see that both d bands narrow, but the band maxima shift little. It remains unclear whether the centroid of each d band in an alloy shifts in the same direction as the core level. X-ray emission experiments may help clarify this issue.[50]

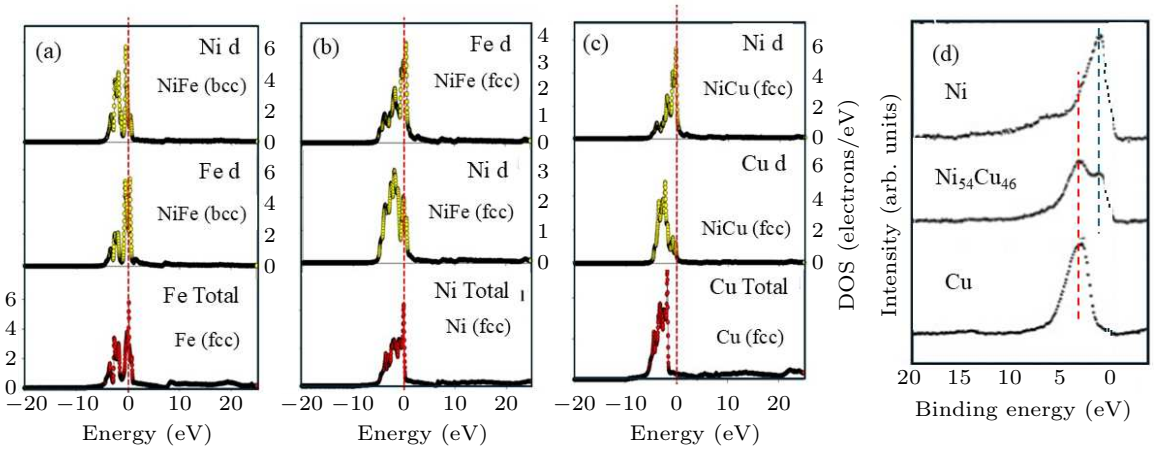


Fig. 5. DOS of the component d bands in 50–50 alloys of NiFe and NiCu together with those of the pure elements. (a) Partial DOS of Ni and Fe in bcc NiFe and the total DOS of bcc Fe. (b) Partial DOS of Ni and Fe d bands in fcc NiFe and the total DOS of fcc Ni. (c) PDOS of Ni and Cu d bands in fcc NiCu and the total DOS of fcc Cu. (d) Photoemission results of Hüfner *et al.* replotted; the vertical lines align the Ni and Cu d-band maxima.[26]

4. Conclusion

The electron redistribution and net charge transfer behavior of Ni–Fe and Ni–Cu alloys are investigated using XRD, XPS, XAS, and DFT band structure calculations. The results are discussed in terms of the strain effect, which can induce intra-atomic s–d rehybridization, and the ligand effect, which involves charge transfer based on the electronegativity difference of the constituents in the alloy. The overall contribution is discussed in the context of the charge compensation model for alloys involving s–d hybridization in transition metals.

The $2p_{3/2}$ core-level shifts observed by XPS show that in the Ni–Fe series, the $2p_{3/2}$ binding energy shifts of Fe and Ni in the alloy are in good accord with electronegativity considerations alone: Fe loses charge and Ni gains charge. Analysis of the strain effect in the absence of charge transfer predicts an opposite trend. Thus, the ligand effect alone can explain the observed binding energy shifts in Ni–Fe alloys, and the strain effect, even in systems with elemental incompatibility in crystal structure for Fe and Ni, is less important than the ligand effect in contributing to the observed BE shift. In Ni–Cu, it is found that the ligand effect is negligible, as predicted, since the electronegativities of Ni and Cu are similar. Tensile strain at the Ni site appears to be less significant than the compressive strain effect at the Cu site, which may influence its electronic behavior by compressing a nearly filled d band.

Review of the ^{57}Fe Mössbauer isomer shift (IS) of Ni–Fe alloys with compositions in the vicinity of that of Invar suggests an increase in s-electron density at the nucleus in the alloy. In contrast to the ligand-effect expectation, this discrepancy can be resolved by the charge compensation model with 3d depletion.

The d-band distribution of 50–50 Ni–Fe and Ni–Cu alloys using DFT calculations shows noticeable overlap of the constituent d bands despite a tendency toward separation in

bcc Ni–Fe. The repulsion is more apparent in the fcc Ni–Fe structure and most pronounced in Ni–Cu. It is interesting to note that while both Fe and Ni occupied d-band edges lie at the Fermi level, in the alloy the Fe d band tends to move towards the Fermi level, and the Ni d band moves away from it. In Ni–Cu, Ni moves towards the Fermi level and Cu moves away from it. Thus, the s–d rehybridization effect and charge compensation in 3d bimetallic alloys are less obvious than in Au(5d)–Cu(3d) and Au(5d)–Al(sp) alloys. This is due to the trend of the disparity between the Slater integrals $F(i,ns)$ and $F(i,(n-1)\mathrm{d})$ from 3d to 5d metals where the effect is the largest in 5d metals, especially Pt and Au. These preliminary discussions show that more investigations are needed to evaluate the significance of strain and ligand effects on s–d hybridization in bimetallic transition-metal alloys. Finally, this study raises questions about the effect of charge compensation in alloying in terms of the interplay between the compressibility of s and d wavefunctions and their effect on the interpretation of spectroscopic observations. Since there has not been systematic work over the last decade, it is hoped that this work will stimulate further discussion moving forward.

Acknowledgments

Research at the University of Western Ontario is supported by NSERC (DG and RTI), CRC, CFI, and OIT, as well as the Canada Research Chair program (TKS). XPS was conducted at Surface Science Western, and the technical assistance of Jeff Henderson is greatly appreciated. The Saskatchewan Structural Sciences Centre (SSSC) is acknowledged for providing facilities to conduct this research. Funding from the Canada Foundation for Innovation, the Natural Sciences and Engineering Research Council of Canada, and the University of Saskatchewan supports research at the SSSC.

References

[1] Silman G I 2012 *Term. Obrab. Metall.* **3** 3
[2] Zhang Y, Zuo T T, Tang Z, Gao M C, Dahmen K A, Liaw P K and Lu Z P 2014 *Prog. Mater. Sci.* **61** 1
[3] Nakamura M, Lee S, Kim J, Park H, Tanaka K and Suzuki Y 2025 *ACS Nano* **5** 196
[4] Chen J, Finfrock Y Z, Wang Z and Sham T K 2021 *Sci. Rep.* **11** 13698
[5] Mankins W L and Lamb S 1990 *ASM Handb.* **2** 428
[6] Meloni E, Martino M and Palma V A 2020 *Catalysts* **10** 352
[7] Wang W, Su C, Wu Y, Ran R and Shao Z 2013 *Chem. Rev.* **113** 8104
[8] Tomishige K, Li D, Tamura M and Nakagawa Y 2017 *Catal. Sci. Technol.* **7** 3952
[9] Shok J and Kawi S 2014 *ACS Catal.* **4** 289
[10] Sahoo A and Medicherla V R R 2021 *Mater. Today* **43** 2242
[11] Waeckerlé T 2010 *IEEE Trans. Magn.* **46** 326
[12] Kittel C 1996 *Introduction to Solid State Physics* 7th edn (New York: Wiley)
[13] Wigner E and Seitz F 1933 *Phys. Rev.* **43** 804
[14] Denton A R and Ashcroft N W 1991 *Phys. Rev. A* **43** 3161
[15] Gelatt Jr. C D, Ehrenreich H and Watson R E 1977 *Phys. Rev. B* **15** 1613
[16] Watson R E and Perlman M L 1974 *Photoelectron Spectrometry*, in *Structure and Bonding* **24** p. 83 (Berlin: Springer)
[17] Watson R E, Perlman M L and Herbst J F 1976 *Phys. Rev. B* **13** 2358
[18] Hodges L, Watson R E and Ehrenreich H 1972 *Phys. Rev. B* **5** 3953
[19] Watson R E, Hudis J and Perlman M L 1971 *Phys. Rev. B* **4** 4139
[20] Pauling L 1930 *The Nature of the Chemical Bond* (Ithaca, NY: Cornell University Press)
[21] Sham T K, Perlman M L and Watson R E 1979 *Phys. Rev. B* **19** 539
[22] Sham T K, Yiu Y M, Kuhn M and Tan K H 1990 *Phys. Rev. B* **41** 11881
[23] Kuhn M, Bzowski A, Sham T K, Rodriguez J A and Hrbek J 1996 *The Solid Films* **283** 209
[24] Sham T K, Perlman M L and Watson R E 1979 *Phys. Rev. B* **20** 3552
[25] Wang D, Cui X, Xiao Q, Hu Y, Wang Z and Sham T K 2008 *AIP Adv.* **8** 065210
[26] Hüfner S, Wertheim G K, Cohen R L and Wernick J H 1972 *Phys. Rev. Lett.* **28** 488
[27] Kistner O C and Sunyar A W 1960 *Phys. Rev. Lett.* **4** 412
[28] Lehlooh A F and Mahmood S H 2002 *Hyperfine Interact.* **139** 387
[29] Kuhn M, Bzowski A and Sham T K 1994 *Hyperfine Interact.* **94** 2267
[30] Watson R E and Perlman M L 1980 *Phys. Scr.* **21** 527
[31] Ohtsu N, Oku M, Shishido T and Wagatsuma K 2007 *Appl. Surf. Sci.* **253** 8713
[32] Skriver H L and Rosengaard N M 1992 *Phys. Rev. B* **46** 7157
[33] Vegard L 1921 *Z. Phys.* **5** 17
[34] Stern E A, Sayers D E and Lytle F W 1975 *Phys. Rev. B* **11** 48
[35] Coulthard I and Sham T K 1996 *Phys. Rev. Lett.* **77** 4824
[36] Sham T K and Carr R 1985 *J. Chem. Phys.* **83** 5914
[37] Hsieh H H, Tsai M S, Lin H J, Chen C T, Wu S C and Hsieh H C 1998 *Phys. Rev. B* **57** 15204
[38] Massalski T B, Okamoto H, Subramanian P R and Kacprzak L 1990 *Binary Alloys Phase Diagrams*, 2nd edn (Metals Park, OH: ASM International)
[39] Fairley N, Barlow A J, Carrick A M R, Roberts M E, Smith J and Wilson R 2021 *Appl. Surf. Sci. Adv.* **5** 100112
[40] *ATENA: XAS Data Processing*
[41] Kohn W and Sham L J 1965 *Phys. Rev.* **140** A1133
[42] Blaha P, Schwarz K, Sorantin P and Trickey S B 1990 *Comput. Phys. Commun.* **59** 399
[43] Yiu Y M 2017 *Applications of Chalcogenides: S, Se, and Te* (Switzerland: Springer)
[44] Materials Project
[45] Perdew J P and Wang Y 1992 *Phys. Rev. B* **45** 13244
[46] Perdew J P, Burke K and Ernzerhof M 1996 *Phys. Rev. Lett.* **77** 3865
[47] Doniach S and Sunjic M 1970 *J. Phys. C Solid State Phys.* **3** 285
[48] Chen J, Li X, Wang Y, Zhang H, Liu Z and Wu Y 2020 *J. Phys. Chem. C* **124** 2313
[49] Valderruten J F, Pérez Alcázar G A and Grenèche J M 2008 *J. Phys. Condens. Matter* **20** 485204
[50] de Groot F M F, Kotani A, van Aken P A and Stavitski E 2024 *Nat. Rev. Methods Primers* **4** 45